Highly anisotropic quasiparticle interference patterns in the spin-density wave state of the iron pnictides

Dheeraj Kumar Singh and Pinaki Majumdar
Harish-Chandra Research Institute, HBNI, Chhatnag Road, Jhunsi, Allahabad 211019, India
(Received 17 April 2017; revised manuscript received 3 October 2017; published 8 December 2017)

We investigate the impurity-scattering-induced quasiparticle interference in the $(\pi,0)$ spin-density wave phase of the iron pnictides. We use a five-orbital tight-binding model and our mean-field theory in the clean limit captures key features of the Fermi surface observed in angle-resolved photoemission. We use a t-matrix formalism to incorporate the effect of doping-induced impurities on this state. The impurities lead to a spatial modulation of the local density of states about the impurity site, with a periodicity of $\sim 8a_{\mathrm{Fe-Fe}}$ along the antiferromagnetic direction. The associated momentum space quasiparticle interference pattern is anisotropic, with major peaks located at $\sim(\pm\pi/4,0)$, consistent with spectroscopic imaging scanning tunneling microscopy. We trace the origin of this pattern to an elliptical contour of constant energy around momentum (0,0), with major axis oriented along the (0,1) direction, in the mean-field electronic structure.

DOI: 10.1103/PhysRevB.96.235111

I. INTRODUCTION

The highly anisotropic electronic properties of the iron pnictides, with broken fourfold rotation symmetry, have been a subject of intense research in recent times. Observed in angle-resolved photoemission spectroscopy [1,2] (ARPES), nuclear magnetic resonance [3] (NMR), and transport properties [4,5], such anisotropy is seen both in the low-temperature collinear antiferromagnetic (AF) state and the high-temperature, unordered, nematic phase [6].

ARPES reveals a significant energy splitting between the d_{xz} and d_{yz} orbitals below the tetragonal-to-orthorhombic transition, which may precede [7] or coincide with [8] the spin-density wave (SDW) transition. The spin dynamics shows a strong twofold anisotropy inside the orthorhombic domains that are formed below the structural phase transition [3], optical spectra displays a significant in-plane anisotropy [9] up to photonic energies $\sim$2 eV, and transport measurements show a larger conductivity in the antiferromagnetic direction compared to the ferromagnetic direction.

Spectroscopic imaging–scanning tunneling microscopy (SI-STM) [10–15] provides insight into the anisotropic electronic state. Quasiparticle interference (QPI) probed by SI-STM measures the modulation of the local density of states (LDOS) induced by the impurity atoms. QPI patterns in the metallic $(\pi,0)$ SDW state consist mainly of a quasi-one-dimensional feature extended along the $q_x = 0$ line with a weaker parallel feature [16–18] at a distance $\sim\pi/4$. Such highly anisotropic features have been attributed to impurity-induced states on the anisotropic magnetic background [19,20].

The QPI probes the response of the ordered state to a strong localized perturbation and several attempts have been made to explain it. A reasonable description of the ARPES and QPI data imposes constraints on the electronic theory of the reference state. Broadly three frameworks have been used to model the QPI, each with some limitation.

(i) In an effective band approach [21] LDOS modulation is strongest along the ferromagnetic direction while experimentally it is in the AF direction. Corresponding contours of constant energy (CCE) consist mainly of a circular pocket around Γ, smaller pockets located inside, and the electron pocket around Y. (ii) A five-orbital model [22] used to study QPI either produces patterns without a clear modulation [23] or shows modulation [24] at an energy $\omega \sim -150$ meV, much larger than in the experiments. (iii) First-principles calculations [25] indicate QPI peaks at $(0, \pm\pi/4)$ and therefore the correct wavelength of modulation, $\sim 8a_{\mathrm{Fe-Fe}}$, but again along the ferromagnetic direction. In this case, FSs consist of a crescentlike structure around Γ with the broader part facing Y. So, either the wavelength, the orientation, or the energy of the QPI modulations remain inconsistent with experiments. It is vital to capture the parallel running satellite peak structures at $(\pm\pi/4,0)$ to reproduce the LDOS modulation of wavelength $\sim 8a_{\mathrm{Fe-Fe}}$ along AF direction.

In this paper, we report on the QPI in the $(\pi,0)$-SDW state of an electron-doped iron pnictide. We use mean-field theory on a five-orbital tight-binding model to describe the ordered state and a t-matrix calculation to quantify (single) impurity effects. We find the following: (i) Our mean-field bands have several features consistent with the ARPES measurements, e.g., a large elliptical pocket around Γ and adjacent four smaller pockets. (ii) The QPI is highly anisotropic, consisting of quasi-one-dimensional peak structures running nearly along $q_x = \pm\pi/4$. (iii) The real-space features consist of LDOS modulation with periodicity $\sim 8a_{\mathrm{Fe-Fe}}$ along the AF direction as observed in the STM measurements. The period of modulation along the AF direction is robust against change in the quasiparticle energy. (iv) Our study also highlights the key role played by the orbital-weight distribution along the reconstructed CCEs.

II. MODEL AND METHOD

In order to study QPI in the SDW state, we consider a five-orbital tight-binding Hamiltonian defined in the Fe-As planes, the kinetic part of which is given by

$$H_0 = \sum_{\mathbf{k}} \sum_{\mu,\nu} \sum_{\sigma} \varepsilon_{\mathbf{k}}^{\mu\nu} d_{\mathbf{k}\mu\sigma}^{\dagger} d_{\mathbf{k}\nu\sigma} \qquad (1)$$

in the plane-wave basis. Here, the operator $d_{\mathbf{k}\mu\sigma}^{\dagger}$ ($d_{\mathbf{k}\mu\sigma}$) creates (destroys) an electron with spin σ and momentum $\mathbf{k}$ in the

μth orbital. Matrix elements $\varepsilon_{\mathbf{k}}^{\mu\nu}$, which include both the hopping matrix elements and the momentum-independent on-site orbital energies, are taken from Ref. [26]. The set of d orbitals, to which orbitals μ and ν belong, consist of $d_{xz}, d_{yz}, d_{xy}, d_{x^2-y^2}$, and $d_{3z^2-r^2}$.

The interaction part includes standard on-site Coulomb interactions

$$H_{\text{int}} = U\sum_{\mathbf{i},\mu} n_{\mathbf{i}\mu\uparrow}n_{\mathbf{i}\mu\downarrow} + \left(U' - \frac{J}{2}\right)\sum_{\mathbf{i},\mu<\nu} n_{\mathbf{i}\mu}n_{\mathbf{i}\nu} - 2J\sum_{\mathbf{i},\mu<\nu}\mathbf{S}_{\mathbf{i}\mu}.\mathbf{S}_{\mathbf{i}\nu} + J\sum_{\mathbf{i},\mu<\nu,\sigma} d^{\dagger}_{\mathbf{i}\mu\sigma}d^{\dagger}_{\mathbf{i}\mu\bar{\sigma}}d_{\mathbf{i}\nu\bar{\sigma}}d_{\mathbf{i}\nu\sigma}. \tag{2}$$

U and U' are the intraorbital and the interorbital Coulomb interaction, respectively. J is the Hund's coupling, with the condition $U' = U - 2J$ imposed for a rotation-invariant interaction.

The mean-field Hamiltonian for the $(\pi,0)$-SDW state in the two-sublattice basis is given by [27]

$$\mathcal{H}_{mf} = \sum_{\mathbf{k}\sigma}\Psi^{\dagger}_{\mathbf{k}\sigma}(\hat{\zeta}_{\mathbf{k}\sigma} + \hat{M}_{\mathbf{k}\sigma})\Psi_{\mathbf{k}\sigma}. \tag{3}$$

$\zeta^{ll'}_{\mathbf{k}\sigma}$ are the matrix elements due to the kinetic part while $M^{ll'}_{\mathbf{k}\sigma} = -s\sigma\Delta_{ll'}\delta^{ll'} + \frac{5J-U}{2}n_{ll'}\delta^{ll'}$. $l, l' \in s\otimes\mu$ with s and μ belonging to the sublattice and orbital bases, respectively. Off-diagonal elements of $\Delta_{ll'}$ and $n_{ll'}$ are small for the parameters considered here, and hence neglected. s and σ in front of $\Delta_{ll'}\delta^{ll'}$ take value 1 (-1) for A (B) sublattice and $\uparrow$-spin ($\downarrow$-spin), respectively. The electron field operator is defined as $\Psi^{\dagger}_{\mathbf{k}\uparrow} = (d^{\dagger}_{A\mathbf{k}1\uparrow}, d^{\dagger}_{A\mathbf{k}2\uparrow}, \ldots, d^{\dagger}_{B\mathbf{k}1\uparrow}, d^{\dagger}_{B\mathbf{k}2\uparrow}, \ldots)$, where subscript indices 1, 2, 3, 4, and 5 stand for orbitals $d_{3z^2-r^2}$, d_{xz}, d_{yz}, $d_{x^2-y^2}$, and d_{xy}, respectively. The exchange fields are given as $2\Delta_{ll} = Um_l + J\sum_{l\neq l'} m_{l'}$. Orbital charge density and magnetization are determined in a self-consistent manner by diagonalizing the Hamiltonian.

The change caused in the Green's function because of a single impurity with δ potential is given by

$$\delta\hat{G}(\mathbf{k},\mathbf{k}',\omega) = \hat{G}^0(\mathbf{k},\omega)\hat{T}(\omega)\hat{G}^0(\mathbf{k}',\omega) \tag{4}$$

using t-matrix approximation. $\hat{G}^0(\mathbf{k},\omega) = [(\omega + i\eta)\hat{\mathbf{I}} - \hat{\mathcal{H}}'_{mf}]^{-1}$ is the Green's function in the SDW state with

$$\hat{\mathcal{H}}'^{\sigma}_{mf} = \begin{pmatrix} \hat{\varepsilon}_{\mathbf{k}} & \text{sgn}\bar{\sigma}\,\hat{\Delta} \\ \text{sgn}\bar{\sigma}\,\hat{\Delta} & \hat{\varepsilon}_{\mathbf{k}+\mathbf{Q}} \end{pmatrix}. \tag{5}$$

$\hat{\mathbf{I}}$ is a 10×10 identity matrix and $\mathbf{Q} = (\pi,0)$. $\hat{\mathcal{H}}'_{mf}$ is obtained from $(\hat{\zeta}_{\mathbf{k}} + \hat{M}_{\mathbf{k}})$ using a unitary transformation [28]. Next,

$$T(\omega) = [\hat{\mathbf{1}} - \hat{V}\hat{\mathcal{G}}^0(\omega)]^{-1}\hat{V}, \tag{6}$$

with

$$\hat{\mathcal{G}}^0(\omega) = \frac{1}{N}\sum_{\mathbf{k}}\hat{G}^0(\mathbf{k},\omega) \tag{7}$$

and

$$\hat{V} = V_{\text{imp}}\begin{pmatrix} \hat{\mathbf{1}} & \hat{\mathbf{1}} \\ \hat{\mathbf{1}} & \hat{\mathbf{1}} \end{pmatrix}. \tag{8}$$

Here, $\hat{\mathbf{1}}$ is a 5×5 identity matrix. Contributions to the change in the DOS is given by $\delta\rho_{\alpha}(\mathbf{q},\omega)$

$$\delta\rho_{\alpha}(\mathbf{q},\omega) = \frac{i}{2\pi}\sum_{\mathbf{k}} g_{\alpha}(\mathbf{k},\mathbf{q},\omega) \tag{9}$$

with

$$\begin{aligned} g_0(\mathbf{k},\mathbf{q},\omega) &= \text{Tr}\delta\hat{G}(\mathbf{k},\mathbf{k}',\omega) - \text{Tr}\delta\hat{G}^*(\mathbf{k}',\mathbf{k},\omega) \\ g_1(\mathbf{k},\mathbf{q},\omega) &= \sum_{\mu\leqslant 5}\delta G_{\mu,\mu+5}(\mathbf{k},\mathbf{k}',\omega) - \delta G^*_{\mu,\mu+5}(\mathbf{k}',\mathbf{k},\omega) \\ g_2(\mathbf{k},\mathbf{q},\omega) &= \sum_{\mu\leqslant 5}\delta G_{\mu+5,\mu}(\mathbf{k},\mathbf{k}',\omega) - \delta G^*_{\mu+5,\mu}(\mathbf{k}',\mathbf{k},\omega), \end{aligned} \tag{10}$$

where $\mathbf{k} - \mathbf{k}' = \mathbf{q}$. Then, the real-space QPI is obtained as

$$\delta\rho(\mathbf{r}_i,\omega) = \frac{1}{N}\sum_{\mathbf{q}}[\delta\rho_0(\mathbf{q},\omega)e^{i\mathbf{q}\cdot\mathbf{r}_i} + \delta\rho_1(\mathbf{q},\omega)e^{i(\mathbf{q}-\mathbf{Q})\cdot\mathbf{r}_i} + \delta\rho_2(\mathbf{q},\omega)e^{i(\mathbf{q}+\mathbf{Q})\cdot\mathbf{r}_i}]. \tag{11}$$

In the following, intraorbital Coulomb interaction parameter (U) is taken as 1.07 eV with $J = 0.25U$ to keep the total magnetic moment per site less than unity. Unlike other studies based on the five-orbital model [23,24], band filling n_e is fixed at 6.03 (3% electron doping) instead of at 6.0. Self-consistently obtained orbital magnetizations are $m_{3r^2-x^2} = 0.086$, $m_{xz} = 0.095$, $m_{yz} = 0.142$, $m_{xy} = 0.186$, and $m_{x^2-y^2} = 0.048$. Orbital charge densities are $n_{3r^2-x^2} = 1.469$, $n_{xz} = 1.208$, $n_{yz} = 1.182$, $n_{xy} = 1.014$, and $n_{x^2-y^2} = 1.158$.

The strength of the impurity potential V_{imp} is chosen to be 200 meV in accordance with density-functional calculations on Co-doped $BaFe_2As_2$ [29]. We have checked in the range $|V_{\text{imp}} - 200\text{ meV}| \leqslant 100$ meV that only the magnitude of the DOS modulation changes while the basic structure of the QPI remains the same. It is to be noted that the LDOS maxima or minima at the impurity site can occur depending on the strength of the impurity potential as shown in a similar study based on a two-orbital model [30]. Further, a mesh size of 300×300 in the momentum space is used for all the calculations.

III. RESULTS

Figures 1(a) and 1(b) show the electronic dispersion and the Fermi surface (FS) in the SDW state. The FS consists of an ellipselike hole pocket around Γ, with major axis in the (0, 1) direction, and tiny electron pockets situated at $\approx (\pm\pi/4,0)$ and $(0,\pm\pi/4)$ but outstretched along (0,1) and (1,0) directions, respectively. Interestingly, similar pockets although larger in size have been reported by the ARPES experiments [31,32]. In addition, there are electron pockets around $(0,\pm\pi)$. Some of the above characteristics of FSs lead to significant anisotropy in the QPI. Figure 1(c) shows that the d_{xy}, d_{yz}, and d_{zx} orbitals dominate at the Fermi level.

In order to understand the QPIs, it will be useful to look at the CCEs of the spectral functions, which are shown in Figs. 2(a)–2(f) as a function of energy with step of 10 meV up to -15 meV starting from -65 meV. Near -65 meV, CCEs consist of an ellipselike pocket P_0 around (0, 0) and two tiny

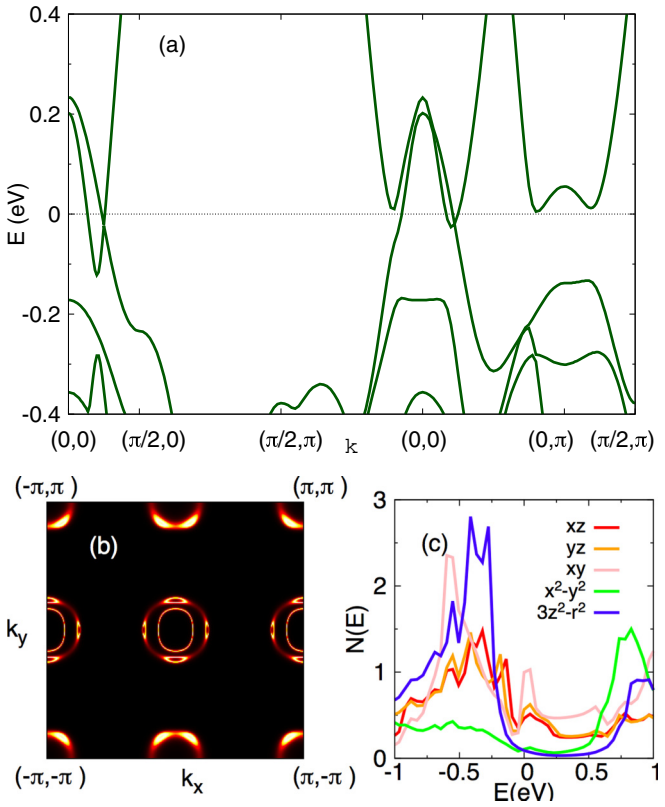

FIG. 1. (a) Electronic dispersion along the high-symmetry directions, (b) reconstructed Fermi surfaces consisting of several pockets near and around Γ as well as around $(\pi,0)$, and (c) orbital-resolved density of states in the $(\pi,0)$-SDW state.

pockets P_1 along $k_y = 0$ mapped onto each other by 180° rotation owing to the C_2 symmetry. Thus, there are four sets of scattering vectors—intrapocket scattering vectors $\mathbf{q}_1$ due to P_0, interpocket scattering vectors $\mathbf{q}_2$ connecting the pockets of P_1, interpocket scattering vectors $\mathbf{q}_3$ connecting P_0 and P_1,

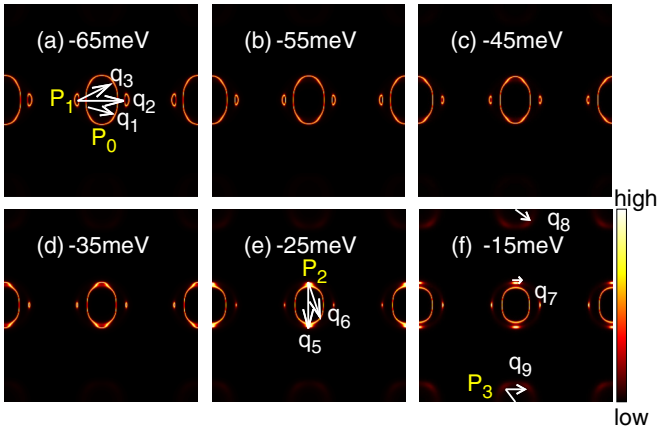

FIG. 2. Constant energy maps of the spectral functions $\mathcal{A}(\mathbf{k},\omega)$ in the unfolded Brillouin zone [k_x and k_y range $(-\pi,\pi)$] from −65 meV (top left) to −15 meV (bottom right) in step of 10 meV. The arrows represent scattering wavevectors in the SDW state. Note that $\mathbf{q}_4$, $\mathbf{q}_7$, and $\mathbf{q}_{10}$ are not shown, which are the intrapocket scattering vectors for the tiny CCEs P_1, P_2, and for the subpockets in CCE P_3, respectively.

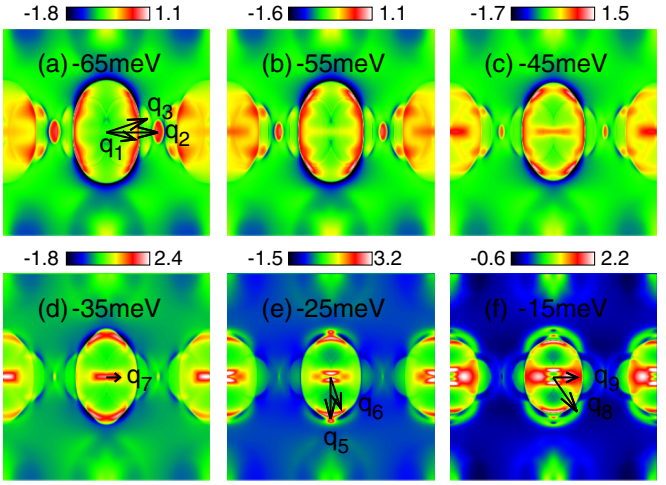

FIG. 3. QPI maps ($\rho_0(\mathbf{q},\omega)$) in the unfolded Brillouin zone [q_x and q_y range $(-\pi,\pi)$] for different energies ω from −65 meV (top left) to −15 meV (bottom right) in steps of 10 meV. The arrows denote the QPI wave vectors in the SDW state.

and intrapocket scattering vectors $\mathbf{q}_4$ [not shown in Fig. 3(a)] due to P_1. Corresponding QPI pattern is expected to have a two-dimensional nature because of a near cancellation of two opposite tendencies in which scattering vectors $\mathbf{q}_1$ try to create a one-dimensional pattern along the (0,1) direction while $\mathbf{q}_2$ and $\mathbf{q}_3$ do the same along the (1,0) direction. On the contrary, the pattern consists of two parallel peak structures running along $q_x = \text{const.}$ and passing through $q_x \approx (\pm\pi/4,0)$ [Fig. 3(a)].

In addition, there are small elliptical pockets located near $q_x \approx (\pm\pi/2,0)$. Here, we note that only those scattering vectors are important, which connect parts of the CCEs having same dominating orbitals because only intraorbital scattering has been incorporated owing to the symmetry consideration [13].

An important change in the QPI patterns occurs upon increasing the energy as shown in Fig. 3(d). This happens primarily because of the appearance of a new set of CCEs in the form of tiny pockets P_2, which emerge out of the elliptical pocket P_0. Since P_2 is in the proximity of band extrema, the pattern generated corresponding to the scattering vectors connecting these pockets should dominate the overall QPI pattern because of a larger phase space available for the scattering processes. Therefore, the balance maintained by the two opposite tendencies described above is perturbed now. This results into a highly anisotropic QPIs [Fig. 3(d)] dominated by wave vectors $\mathbf{q}_5$, $\mathbf{q}_6$, and $\mathbf{q}_7$ [Fig. 3(c)] . $\mathbf{q}_5$ and $\mathbf{q}_7$ are the set of interpocket and intrapocket scattering vectors for P_2 pockets, respectively, whereas $\mathbf{q}_6$ is another set of interpocket scattering vectors connecting P_0 and P_2.

On increasing energy further, an additional set of CCEs appear near $(0, \pm\pi)$ as seen Fig. 2(f), which may also contains very small subpockets [Fig. 1(b)]. As these are in the vicinity of local band extrema and parallel to the $k_y = 0$, two-dimensional characteristics is imparted to the QPIs as noticed in Fig. 3(f). Dominating QPI wave vectors are due to the intersubpocket scattering vectors $\mathbf{q}_8$ and $\mathbf{q}_9$ as well as due to intrasubpocket scattering vectors $\mathbf{q}_{10}$ not shown [Fig. 1(b)].

Several aspects of the QPI obtained here compare well with those of SI-STM measurements carried out for $Ca(Fe_{1-x}Co_x)_2As_2$. For $\omega = -35$ meV, a central peak structure runs along $q_x = 0$ and consists of three main peaks, which themselves are made of multiple peaks either coinciding or placed very closely: one at (0, 0), and other two placed equidistant from it. Additionally, there are parallel running satellite peak structures situated at $\approx (\pm\pi/4,0)$, which are part of an elliptical QPI patterns. The quasi-one-dimensional nature of the pattern is found in a wide energy window. These features are in agreement with the STM measurements. We also note that they are very sensitive to energy as evident from Fig. 3(e), when they become very weak for $\omega = -15$ meV on increasing the quasiparticle energy further. Features of the CCEs especially the existence of pockets along $k_x = 0$, which play a crucial role in imparting the quasi-one-dimensionality to the main peak structure, have also been noticed in the ARPES measurements. We have also examined the role of an orbital splitting term in the Hamiltonian, which is found to bring in only minor deviations because of a relatively large sized P_1 and also due to the suppression of pockets P_2. Thus, it is the significant band reconstruction in the SDW state, which is responsible for the experimentally observed anisotropy in the QPI.

Figure 4 shows corresponding real-space QPI pattern, which has been obtained by the Fourier transform of momentum-space QPI [Eq. (11)]. For a better visibility, particularly in the immediate vicinity of the impurity atom, modulation on the lattice size 80×80 with the impurity atom at the center is presented though the result is obtained on the lattice size 300×300.

The wavelength of LDOS modulation along x (antiferromagnetic direction) is $R_x \sim 8a_{\mathrm{Fe-Fe}}$ for all energy values considered here though modulation may be weak or strong depending on the energy. A strong modulation along x is seen for energies $\omega = -65$ meV and -55 meV, with parallel running peak structures along $q_x = $ const. and passing through $q_x = 2\pi/R_x \approx (\pm\pi/4,0)$ in qualitative agreement with the impurity-induced electronic structure observed by the SI-STM experiments. However, it becomes stronger along $x \approx y$ upon increasing the energy and corresponds to a strong modulation of DOS in the momentum space along a direction tilted away from $q_x = $ const. Further, three dark spots aligned along the ferromagnetic direction can be clearly seen in the vicinity of impurity as quasiparticle energy crosses $\omega = -0.045$ meV. The feature with a distance of $\approx 6a_{\mathrm{Fe-Fe}}$ between two consecutive dark spots gets pronounced as $\omega = -0.015$ meV is approached.

IV. DISCUSSION

A. Physical mechanism

Our study highlights the role of redistributed orbital weight along the CCEs. In the unordered state, the hole pockets around Γ have predominantly d_{xz} and d_{yz} character distributed in a way to respect the fourfold rotational symmetry. On the contrary, the CCE pocket around Γ in the SDW state is dominated by the d_{xz} orbital. For $\omega = -65$ meV, the scattering vectors connecting the regions near the vertices along the minor axis of elliptical pocket leads to the most intense region in the QPI. This happens primarily because of two reasons.

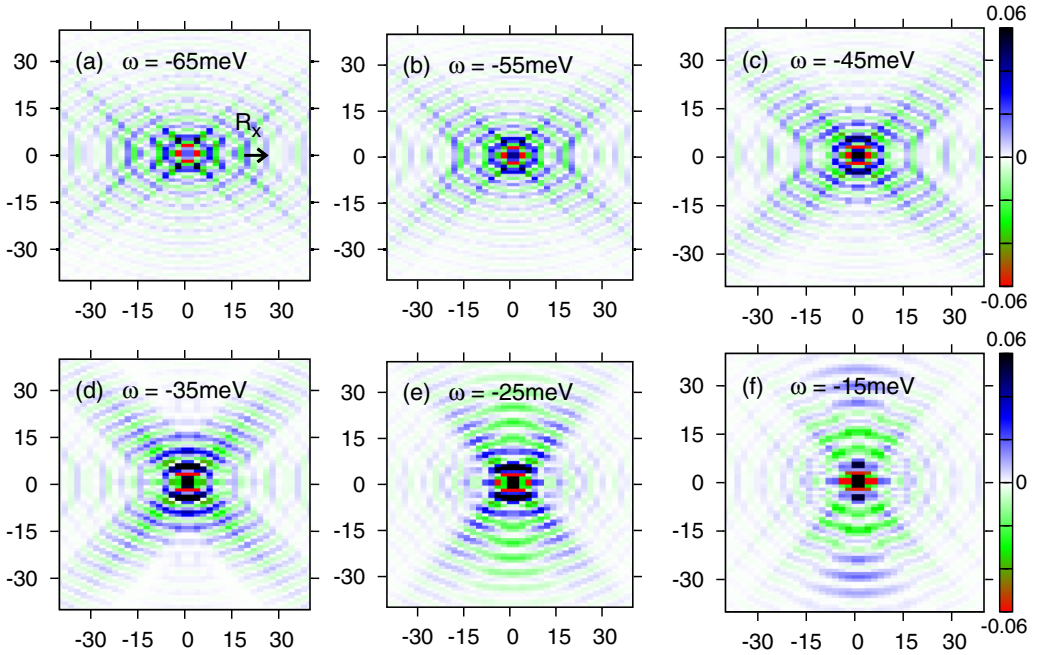

FIG. 4. Real-space QPIs for the set of parameters as in Fig. 3. For better visibility, LDOS modulation on the lattice size 80×80 with impurity at the center is shown whereas the results are obtained for lattice size 300×300. LDOS modulation along the antiferromagnetic direction (x axis) with the wavelength $R_x \approx 8a_{\mathrm{Fe-Fe}}$. Although the period of modulation along the antiferromagnetic direction remains almost unchanged, the strong modulation direction is sensitive to the quasiparticle energy.

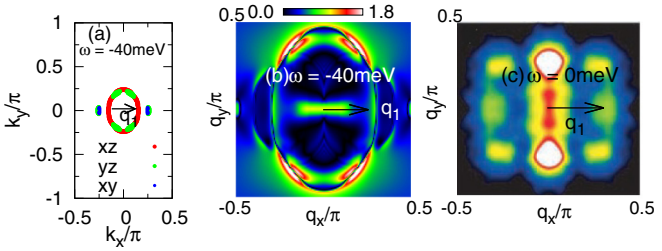

FIG. 5. (a) CCEs for $\omega = -40$ meV with dominant orbital character in the SDW state and (b) corresponding absolute value of momentum-space QPI modulations. (c) QPI patterns observed in 3% electron-doped $CaFe_2As_2$ for $\omega = 0$ meV by the STM [16].

First, a larger phase space is available when compared with the case of scattering vectors connecting the vertices along the major axis. Second, only intraorbital scattering processes are taken into account. On increasing energy, a small d_{yz}-rich region [Fig. 5(a)] appears along the elliptical CCE as a new band crosses the quasiparticle energy. Because of the new band's extrema and associated large spectral weight, QPI pattern due to the scattering vectors connecting d_{yz}-rich regions prevails over the others [Fig. 5(b)]. Consequently, the most intense region moves towards the vertices along the major axis [Figs. 3(b)–3(d)] a features present also in the STM results [Fig. 5(c)].

In this work, the focus was on the LDOS modulation. Another important issue is the modulation in the local magnetization induced in the vicinity of the impurity. This has been addressed in a recent work within a self-consistent approach for single nonmagnetic impurity [20]. The study found that the impurity induces magnetic nanostructures with checkerboard-type order inside, extended along the antiferromagnetic direction with a significant LDOS modulation at the ends. Our result on the LDOS modulation in real space is also consistent with this study.

B. Comparison with earlier work

Anisotropy in the QPI patterns of the SDW state is not unexpected because of the breaking of fourfold rotational symmetry. However, the details of the patterns depend on the electronic structure. A plausible description of the QPI patterns constrains the modeling of the electronic structure. Additional constraint comes from the ARPES measurement, which, for instance in the undoped case, is suggestive of a large pocket around (0, 0) and other smaller adjacent pockets along $k_x, k_y = 0$. Those along $k_x = 0$ appear to be the smallest and with large spectral density [31]. The CCEs in the electron-doped pnictides for any investigation of QPIs are expected to show at least a qualitative agreement with the ARPES results.

An important advantage of the band model is the control on the ellipticity of the electron pocket at $(\pm\pi,0)$ in the unordered state [33]. However, reconstructed bands consist, apart from the circular pockets around (0, 0), of additional adjacent small pockets along $k_y = 0$ but extended along (0, 1) with large spectral density, which is responsible for the strong modulation in the ferromagnetic direction instead [21]. Another important limitation of this approach is its inability to capture the orbital-weight distribution, which can provide not only the physical origin of the transport anisotropy but is also helpful in describing some of the essential features of the QPI patterns as highlighted in this paper.

One of the studies based on the five-orbital model of Graser *et al.* [22] while focusing on differentiating signatures of orbital splitting and antiferromagnetic gaps found the QPI patterns [23], despite showing a certain degree of anisotropy, to be peaked uniformly in a large part of the Brillouin zone. Consequently, the real-space pattern did not have the LDOS modulation along the antiferromagnetic direction with periodicity $\sim 8a_{\mathrm{Fe-Fe}}$. Similarly, another study based on the same model but concentrating on features associated with the nematicity, found a quasi-one-dimensional peak structure along $q_x = 0$ in the SDW state [24]. However, the strongest peak appears near $\mathbf{q} = (0,0)$. Further, the parallel running peak structures along $q_x \approx \pm\pi/4$ are also absent. Corresponding CCEs, particularly near (0, 0) are rather extended along (1, 0) direction nearly up to the zone boundary, which has not been observed so far in the ARPES measurements. This is perhaps due to a large energy $\omega \sim -150$ meV considered. In this study, real-space LDOS modulation was not presented, which is again expected to miss the periodic modulation along the antiferromagnetic direction with periodicity $\sim 8a_{\mathrm{Fe-Fe}}$.

In another study based on first-principles calculations of the electronic structure in the SDW state [25], reconstructed Fermi pockets consisted of crescentlike pockets around Γ with the broader part facing Y, which resulted in QPI patterns having similar structure. Thus, neither the Fermi pockets nor the QPI patterns agree with the experiments, in particular, latter will consist of a modulation along the ferromagnetic direction.

Therefore, the failure of almost all the earlier work (Table I) in reproducing the nearly parallel running satellite peak structures along $q_x \approx \pm\pi/4$ highlights the limitation of the electronic structure used. In our work, on the other hand, these structures result from the elliptical CCE around (0,0) with a major role played by the scattering vectors lying nearly parallel to the minor axis of length $\sim\pi/4$. Further, the extremum of a new band crossing the quasiparticle energy and associated large spectral density also has an important role in the QPI. The CCEs associated with this band transform to pockets near the vertices along the major axis of the large elliptical pocket and correspond to the adjacent electron pocket observed in the ARPES measurements. We believe that the Fermi pocket around Γ, the existence of which has also been suggested by the ARPES measurements, is likely to be elliptical in shape.

C. Unresolved issues

For 3% doping on the parent state the $8a_{\mathrm{Fe-Fe}} \times 8a_{\mathrm{Fe-Fe}}$ nanostructures would contain more than one impurity atom on the average. Therefore, the interference between scattering events from multiple impurities could be important for the measured QPI patterns. The present t-matrix approach unfortunately does not access these effects. Recently, a framework to study QPI in the presence of interacting multiple impurities has been discussed [34]. However, in many instances, single impurity treatment has yielded QPI patterns, which successfully describe the qualitative features of STM measurements. The

TABLE I. A comparison of QPI characteristics obtained in various studies with those obtained in SI-STM.

Model	Focus	Quasi-one-dimensional peak structures near $(\pm\pi/4,0)$ in **k**-space QPI	LDOS modulation along the antiferromagnetic direction with periodicity $\sim 8a_{\mathrm{Fe-Fe}}$
Effective band model [21]	SDW state	Weak one-dimensional features	Yes, but strongest modulation along FM direction
Five-orbital model [23]	Orbital anisotropy (QPIs only near T_N)	No	No strong modulation along any specific direction
Five-orbital model [24]	Nematicity (and SDW state)	No [only at (0,0)]	—
First-principles calculation [25]	SDW state	No (structure rotated by 90°)	—
This work	SDW state	Yes	Yes

LDOS modulation obtained in this work with the periodicity $\sim 8a_{\mathrm{Fe-Fe}}$ is another such example.

LDOS modulation with the experimentally observed periodicity is reproduced successfully in our results along the antiferromagnetic direction, and is robust against any change in the quasiparticle energy. However, the strongly modulated direction exhibits sensitivity to the quasiparticle energy, which is due to the fast change in the CCEs. In the experiments, however, the strongly modulated direction is robustly along the antiferromagnetic direction despite the change in energy. This may indicate that CCEs change comparatively slowly in the real systems as a function of energy.

V. CONCLUSIONS

We have investigated the quasiparticle interference pattern in the $(\pi,0)$-SDW state using a five-orbital tight-binding model of electron-doped iron pnictides. With a realistic reconstructed band structure, which includes an ellipselike constant energy contour around (0, 0) and additional nearby smaller pockets, we find highly anisotropic QPI patterns. Because the scattering vectors oriented along the minor axis of the elliptical CCE (of length $\pi/4$) connects d_{xz}-rich segments, QPI peak structures are obtained at $\approx(\pm\pi/4,0)$, running parallel to the q_y axis. The corresponding real-space pattern consists of LDOS modulation along the antiferromagnetic direction with periodicity $\sim 8a_{\mathrm{Fe-Fe}}$. Both the features are in agreement with STM results for the doped iron pnictides.

ACKNOWLEDGMENT

We acknowledge use of the HPC Clusters at HRI.

[1] M. Yi, D. Lu, J.-H. Chu, J. G. Analytis, A. P. Sorini, A. F. Kemper, B. Moritz, S.-K. Mo, R. G. Moore, M. Hashimoto, W.-S. Lee, Z. Hussain, T. P. Devereaux, I. R. Fisher, and Z.-X. Shen, Proc. Natl. Acad. Sci. USA **108**, 6878 (2011).

[2] T. Shimojima, K. Ishizaka, Y. Ishida, N. Katayama, K. Ohgushi, T. Kiss, M. Okawa, T. Togashi, X.-Y. Wang, C.-T. Chen, S. Watanabe, R. Kadota, T. Oguchi, A. Chainani, and S. Shin, Phys. Rev. Lett. **104**, 057002 (2010).

[3] M. Fu, D. A. Torchetti, T. Imai, F. L. Ning, J.-Q. Yan, and A. S. Sefat, Phys. Rev. Lett. **109**, 247001 (2012).

[4] J.-H. Chu, J.-H. Chu, J. G. Analytis, K. De Greve, P. L. McMahon, Z. Islam, Y. Yamamoto, and I. R. Fisher, Science **329**, 824 (2010).

[5] M. A. Tanatar, E. C. Blomberg, A. Kreyssig, M. G. Kim, N. Ni, A. Thaler, S. L. Bud'ko, P. C. Canfield, A. I. Goldman, I. I. Mazin, and R. Prozorov, Phys. Rev. B **81**, 184508 (2010).

[6] E. C. Blomberg, M. A. Tanatar, R. M. Fernandes, I. I. Mazin, B. Shen, H.-H. Wen, M. D. Johannes, J. Schmalian, and R. Prozorov, Nat. Commun. **4**, 1914 (2013).

[7] S. Nandi, M. G. Kim, A. Kreyssig, R. M. Fernandes, D. K. Pratt, A. Thaler, N. Ni, S. L. Budko, P. C. Canfield, J. Schmalian, R. J. McQueeney, and A. I. Goldman, Phys. Rev. Lett. **104**, 057006 (2010).

[8] M. Rotter, M. Tegel, D. Johrendt, I. Schellenberg, W. Hermes, and R. Pöttgen, Phys. Rev. B **78**, 020503R (2008).

[9] M. Nakajima, T. Liang, S. Ishida, Y. Tomioka, K. Kihou, C. H. Lee, A. Iyo, H. Eisaki, T. Kakeshita, T. Ito, and S. Uchida, Proc. Natl. Acad. Sci. USA **108**, 12238 (2011).

[10] L. Capriotti, D. J. Scalapino, and R. D. Sedgewick, Phys. Rev. B **68**, 014508 (2003).

[11] S. Sykora and P. Coleman, Phys. Rev. B **84**, 054501 (2011).

[12] A. Kreisel, Peayush Choubey, T. Berlijn, W. Ku, B. M. Andersen, and P. J. Hirschfeld, Phys. Rev. Lett. **114**, 217002 (2015).

[13] Y.-Y. Zhang, C. Fang, X. Zhou, K. Seo, W.-F. Tsai, B. A. Bernevig, and J. Hu, Phys. Rev. B **80**, 094528 (2009).

[14] Y. Yamakawa and H. Kontani, Phys. Rev. B **92**, 045124 (2015).

[15] P. J. Hirschfeld, D. Altenfeld, I. Eremin, and I. I. Mazin, Phys. Rev. B **92**, 184513 (2015).

[16] T.-M. Chuang, M. P. Allan, J. Lee, Y. Xie, N. Ni, S. L. Budko, G. S. Boebinger, P. C. Canfield, and J. C. Davis, Science **327**, 181 (2010).

[17] E. P. Rosenthal, E. F. Andrade, C. J. Arguello, R. M. Fernandes, L. Y. Xing, X. C. Wang, C. Q. Jin, A. J. Millis, and A. N. Pasupathy, Nat. Phys. **10**, 225 (2014).

[18] X. Zhou, C. Ye, P. Cai, X. Wang, X. Chen, and Y. Wang, Phys. Rev. Lett. **106**, 087001 (2011).

[19] M. P. Allan, T.-M. Chuang, F. Massee, Yang Xie, Ni Ni, S. L. Budko, G. S. Boebinger, Q. Wang, D. S. Dessau, P. C. Canfield, M. S. Golden, and J. C. Davis, Nat. Phys. **9**, 220 (2013).

[20] M. N. Gastiasoro, P. J. Hirschfeld, and B. M. Andersen, Phys. Rev. B **89**, 100502 (2014).
[21] J. Knolle, I. Eremin, A. Akbari, and R. Moessner, Phys. Rev. Lett. **104**, 257001 (2010).
[22] S. Graser, T. A. Maier, P. J. Hirschfeld, and D. J. Scalapino, New J. Phys. **11**, 025016 (2009).
[23] N. Plonka, A. F. Kemper, S. Graser, A. P. Kampf, and T. P. Devereaux, Phys. Rev. B **88**, 174518 (2013).
[24] H.-Y. Zhang and J.-X. Li, Phys. Rev. B **94**, 075153 (2016).
[25] I. I. Mazin, S. A. J. Kimber, and D. N. Argyriou, Phys. Rev. B **83**, 052501 (2011).
[26] H. Ikeda, R. Arita, and J. Kunes, Phys. Rev. B **81**, 054502 (2010).
[27] S. Ghosh and A. Singh, New J. Phys. **17**, 063009 (2015).
[28] D. K. Singh and T. Takimoto, J. Phys. Soc. Jpn. **85**, 044703 (2016).
[29] A. F. Kemper, C. Cao, P. J. Hirschfeld, and H.-P. Cheng, Phys. Rev. B **80**, 104511 (2009).
[30] H. Huang, Y. Gao, D. Zhang, and C. S. Ting, Phys. Rev. B **84**, 134507 (2011).
[31] M. Yi, D. H. Lu, J. G. Analytis, J.-H. Chu, S.-K. Mo, R.-H. He, M. Hashimoto, R. G. Moore, I. I. Mazin, D. J. Singh, Z. Hussain, I. R. Fisher, and Z.-X. Shen, Phys. Rev. B **80**, 174510 (2009).
[32] Q. Wang, Z. Sun, E. Rotenberg, F. Ronning, E. D. Bauer, H. Lin, R. S. Markiewicz, M. Lindroos, B. Barbiellini, A. Bansil, and D. S. Dessau, arXiv:1009.0271.
[33] I. Eremin and A. V. Chubukov, Phys. Rev. B **81**, 024511 (2010).
[34] A. K. Mitchell, P. G. Derry, and D. E. Logan, Phys. Rev. B **91**, 235127 (2015).